Research Article Vol. 27, No. 21 / 14 October 2019 / *Optics Express* 30763

Optics EXPRESS

Indium antimonide uncooled photodetector with dual band photoresponse in the infrared and millimeter wave range

JINCHAO TONG,[1,6] FEI SUO,[1] WEI ZHOU,[2] YUE QU,[2] NIANGJUAN YAO,[2] TAO HU,[2] ZHIMING HUANG,[2,3,5] AND DAO HUA ZHANG[1,4]

[1] *School of Electrical and Electronic Engineering, Nanyang Technological University, Nanyang Avenue, 639798, Singapore*
[2] *State Key Laboratory of Infrared Physics, Shanghai Institute of Technical Physics, Chinese Academy of Sciences, 500 Yu Tian Road, 200083, Shanghai, China*
[3] *Key Laboratory of Space Active Opto-Electronics Technology, Shanghai Institute of Technical Physics, Chinese Academy of Sciences, 500 Yu Tian Road, 200083, Shanghai, China*
[4] *edhzhang@ntu.edu.sg*
[5] *zmhuang@mail.sitp.ac.cn*
[6] *jctong@ntu.edu.sg*

Abstract: All-InSb film-based and spiral antenna-assisted Au-InSb-Au metal-semiconductor-metal detector is reported with dual-band photoresponse in the infrared (IR) and millimeter wave range. At IR, the detector exhibits a long wavelength 100% cut-off at 7.3 µm. Under an applied bias of 5 mA, the uncooled blackbody responsivity and specific detectivity are 3.5 A/W and 1×10^8 Jones, respectively. The $f_{-3\mathrm{dB}}$ value measured at 2.94 µm is 75 KHz, corresponding to a detector rise speed of 4.7 µs. At millimeter wave range, the detector shows a narrowband response determined by the coupling of the antenna. A voltage responsivity of 25 V/W is achieved at 167 GHz (1.796 mm) under an applied bias of 25 mA, and the corresponding noise equivalent power (NEP) is 1.0×10^{-10} WHz$^{-1/2}$, which can be improved to 1.8×10^{-12} WHz$^{-1/2}$ if normalized to the real active semiconductor area. A $f_{-3\mathrm{dB}}$ value of 17.5 KHz, corresponding to a detector rise speed of 20 µs is achieved in this range. A proof of principle for IR-modulated photoresponse for millimeter wave is achieved with a maximum modulation depth of 47.5%. This All-InSb film-based detector and the modulation are promising for future novel optoelectronic devices in IR and millimeter waves.

1. Introduction

Photodetector with multiband capacity is regarded as the next generation of development. Current technologies mainly depend on mercury cadmium telluride (HgCdTe), quantum well infrared photodetectors (QWIPs), antimonide based type II superlattice, quantum cascade detectors (QCDs), and quantum dot infrared photodetectors (QDIPs) from short wave (SWIR) to middle wave (MWIR) and long wave infrared (LWIR) [1]. Recently, XBn structures with high detecting performance for IR have also been reported [2,3]. Photodetectors being able to simultaneously detect IR and millimeter waves would be highly desirable for wide spectral information acquisition. Current mature IR photodetectors (e.g., InGaAs, HgCdTe, type II, QCDs, QDIPs, and QWIPs) show intrinsically a selective wavelength dependence of response [4–11]. To cause excitation of photocarriers, the photons impinging on the semiconductor must have enough quantum energy to excite interband, intersubband or impurity band transition of electrons, which makes multiband photodetection from IR to millimeter wave notoriously difficult. This dilemma mainly originates from difficulty in achieving sensitive photodetection of long wavelength radiations (with extremely low photon energies, e.g., millimeter wave, 2 mm@0.621 meV) by using

#374458 https://doi.org/10.1364/OE.27.030763
Journal © 2019 Received 1 Aug 2019; revised 17 Sep 2019; accepted 26 Sep 2019; published 9 Oct 2019

conventional optoelectronic semiconductors if still relying on characteristic bandgap transitions. This is because the bandgaps of these semiconductors are much larger than quantum energies of long wavelength photons. In addition, the strong thermal noise (~k_BT, 25.6 meV at room temperature) from background has significant disturbance.

Currently, commercially available Golay cells, pyroelectric elements, bolometers, Schottky barrier diodes (SBDs), and photoconductive antenna (PCs) receivers are widely used for millimeter wave detection [12–16]. Based on thermal sensing mechanisms, the first three either suffer from slow response (millisecond level for Golay cells and pyroelectric elements) or require cryogenic cooling for normal operation (4.2 K for typical Si bolometers). SBDs, widely used in radio-frequency (RF) and microwave ranges, are high speed but require advanced fabrication and material growth techniques. PC receivers have been very successfully and maturely used in terahertz time domain systems (THz-TDS). It requires a local femtosecond laser to pump the semiconductor located in the center of a coupling antenna.

Sensitive long wavelength photodetection based on surface plasmon induced non-equilibrium electrons in high-mobility semiconductor has been reported [17]. Based on this strategy, subwavelength ohmic Au-InSb-Au two-terminal detectors have demonstrated extremely high sensitivity at 37.5 GHz (8 mm) and 330 GHz (0.9 mm), equipped with appropriate coupling antennas [17]. As InSb is also well-known for its widespread application in IR detection (e.g., liquid nitrogen cooled focal plane arrays [18]), it is possible to develop InSb-based dual band photodetectors which have photoresponse for both IR and millimeter waves.

In this work, we study an all InSb film-based uncooled metal-semiconductor-metal (MSM) detector in detecting IR and millimeter waves. The detecting performance of this detector has been characterized in detail in both electromagnetic wave ranges. The simple detector design exhibits comparable uncooled detecting performance to commercial counterparts in each range. A proof of principle for IR modulated photoresponse for millimeter wave has also been realized by tailing plasmonic effect in the detector. This work offers a pathway to develop dual-band photodetector and other novel optoelectronic devices in IR and millimeter waves.

2. Results and discussions

The detector is based on metal-semiconductor-metal structure, wherein a planar Au spiral antenna is used to couple radiations within specific wavelength range (Fig. 1(a)). Under external millimeter irradiation, the planar antenna can efficiently couple the photons into the central MSM structure, where as InSb is a plasmonic semiconductor in millimeter wave range [19–22], localized surface plasmon polaritons (LSPs) will be excited. Thereafter, non-equilibrium electrons will be induced through decaying of those LSPs, leading to unidirectional photocurrent under external bias [17]. Previously, we have adopted planar dipole and log-period antennas to couple millimeter wave radiations into the MSM structure [17,23]. The design of these antennas was carried out by Comsol and HFSS software. They are optimized for efficiently coupling radiations within specific wavelength range. Meanwhile, they should be ohmic contact with the semiconductors used in the structure to allow successful collection of carriers. In microwave and millimeter wave range, another type of planar antenna, named spiral antenna, is also widely used for coupling radiations. Their design and optimization strategy have been reported previously [24–27]. Here, we design the spiral antenna following these early reports with scaled geometrical size for efficiently coupling radiations at around 167 GHz (1.796 mm). The length (l) and width (m) of the antenna are 0.9 mm and 0.6 mm, respectively. After determining the coupling antenna, we also need to consider the InSb photoconductive design in the MSM structure. To allow enough space for ohmic contact with the antenna, reasonable active absorption area for IR waves, large LSPs generation, and suitable resistance in our measurements, the final determined InSb mesa in the central portion of the antenna has a length p, thickness n, and lateral width of 130 µm, 10 µm and 50 µm, respectively. Two ohmic metallic contacts are formed on InSb with a spacing s of 90 μm (Fig. 1(b)). In detector fabrication, single crystal undoped InSb (111) was used. It was first transferred and affixed on to a sapphire substrate by epoxy glue. Then, it was polished into a 10 μm thick film. Conventional ultraviolet photolithography and wet etching process (HF: HAC: H_2O_2) were adopted to define the central InSb mesa. The ohmic metallic contacts and spiral antenna were then defined via ultraviolet photolithography, e-beam evaporation, and standard lift-off. The metallic ohmic contacts and spiral antenna include 15 nm Cr adhesion layer and 400 nm Au. The SEM of the finally fabricated detector is shown in Fig. 1(c).

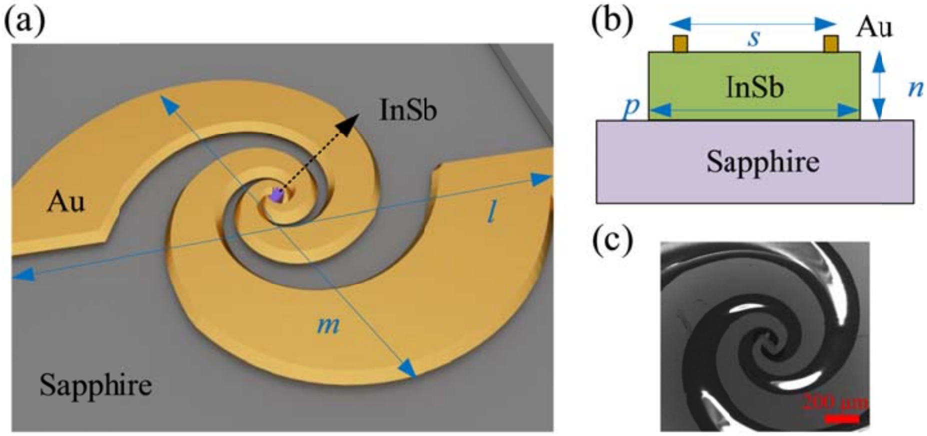

Fig. 1. (a) Schematic of the InSb-based dual-band photodetector on sapphire substrate. (b) Cross-section of the central Au-InSb-Au MSM. (c) The SEM of the detector. The scale bar represents 200 μm.

The spectral response of the detector at IR was measured using a standard Fourier Transform Infrared Spectroscopy (FTIR) system. The light from the IR source was focused onto the detector sample located at the external port. A IR KBr beam splitter (BMS) and a standard calibrated DTGS detector were used in experiments. A 1000 K blackbody source was used to evaluate the blackbody responsivity and specific detectivity of the detector at IR with a modulation frequency of 2 KHz and field of view π. To make it more convenient to compare with other IR detectors, here we characterized the responsivity by A/W. A 2.94 μm IR source with maximum modulation frequency of 1 MHz was used to obtain the response waveform and $f_{-3\mathrm{dB}}$ value of the detector at IR. For millimeter wave measurements (see Fig. 2), a commercial VDI source was used for irradiations from 164 GHz to 174 GHz. It was electrically modulated before incident onto the detector. The detector was biased with a direct current. The photovoltage or photocurrent signal was first amplified and then recorded by a lock-in amplifier or oscilloscope. A Golay cell was used to calibrate the responsivity as

$$R = V/(pA) = VA_G R_G/(V_G A), \tag{1}$$

where p is the power density, V and V_G are the photovoltage of the dual-band detector and Golay cell, respectively (here we adopted V/W as usual for millimeter wave detectors), A is the effective absorption area of the detector, described as $A = G\lambda^2/(4\pi)$ (G is the gain of the antenna and assuming it is matched to its load) [28], A_G is the absorption area of the Golay cell (50 mm^2), and R_G is the responsivity of the Golay cell (~10^5 V $\mathrm{W0}^{-1}$ at 15 Hz and room temperature). It is noted here that the absorption area in IR range equals to the real active semiconductor area (4500 $\mu\mathrm{m}^2$) of the detector. But for long wavelength millimeter waves, the absorption should be accounted with the effective absorption area of the antenna (~0.2478 mm^2 if assuming $G = 1$) due to its coupling. From the perspective of real millimeter applications, the figure of merit utilized to evaluate the performance of a detector is the noise equivalent power (NEP), which corresponds to the lowest detectable power in a 1 Hz bandwidth. The lower the NEP, the better the performance of the detector. NEP can be expressed as [29]

$$NEP = v_n/R, \tag{2}$$

where v_n is the root mean square (RMS) of the noise voltage, and R is the voltage responsivity of the detector. For our detector, in addition to the thermal Johnson-Nyquist noise (v_t), the noise (v_b) due to bias (dark current) should also be included. The total noise can be described by [1,30]

$$v_n = (v_t{}^2 + v_b{}^2)^{1/2} = (4k_BTr + 2qI_dr^2)^{1/2}, \tag{3}$$

where k_B is Boltzmann's constant in joules per kelvin, T is the detector's absolute temperature in kelvin, r is the resistance value of the device in ohms (Ω), q is the elementary charge, and I_d is the dark current of the device (bias current in our case). A spectrum analyzer was also used to confirm the noise level of the detector.

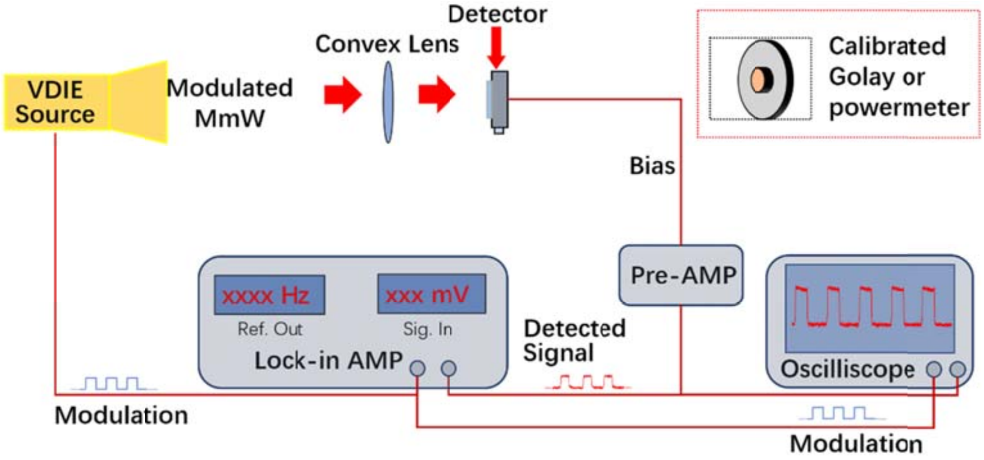

Fig. 2. Schematic of measurement set-up for millimeter wave.

Figure 3(a) shows the relative spectral response of the detector in IR range. It has a long wavelength 100% cutoff at 7.3 µm, corresponding to the bandgap energy of 0.17 eV for InSb at room temperature. The reduction at short wavelength is mainly due to the surface recombination of carriers [31]. The inset shows the typical current-voltage (I-V) characteristic curve of the detector. The excellent linearity and symmetry demonstrate the good ohmic contact between metals and InSb. The derived resistance of the detector is ~30 Ω. The blackbody responsivity (Fig. 3(b)) increases as increasing bias current owing to increased photoconductive gain, which is typical for a photoconductor [1]. Specifically, a photocurrent responsivity of 3.5 A/W is achieved under a bias current of 5 mA. The corresponding blackbody specific detectivity is nearly 1×10^8 Jones (Fig. 3(c)), which is comparable to the commercial thermoelectric cooled InSb photoconductor counterpart [32]. To evaluate the response speed (including the measurement circuit) of the device at IR, we used a 2.94 µm source with maximum modulation frequency up to 1 MHz. The rise and fall time of the square wave source is 20 ns. The output power of the source is found to be stable at all modulation frequencies. Figure 3(d) shows the normalized amplitude-frequency response of the detector under 5 mA bias. As shown, the $f_{-3\mathrm{dB}}$ of the detector is approximately 75 KHz [33], corresponding to a rise time of 4.7 µs according to t_r=0.35/$f_{-3\mathrm{dB}}$, which is close to the rise time (~4.1 µs) directly observed from the response waveform as shown in time-domain measurements (Figs. 3(e) and 3(f)). This response speed is also in agreement with the reported value of carrier lifetime [34]. But it is slower than that of the commercial InSb photoconductor at low temperatures [32].

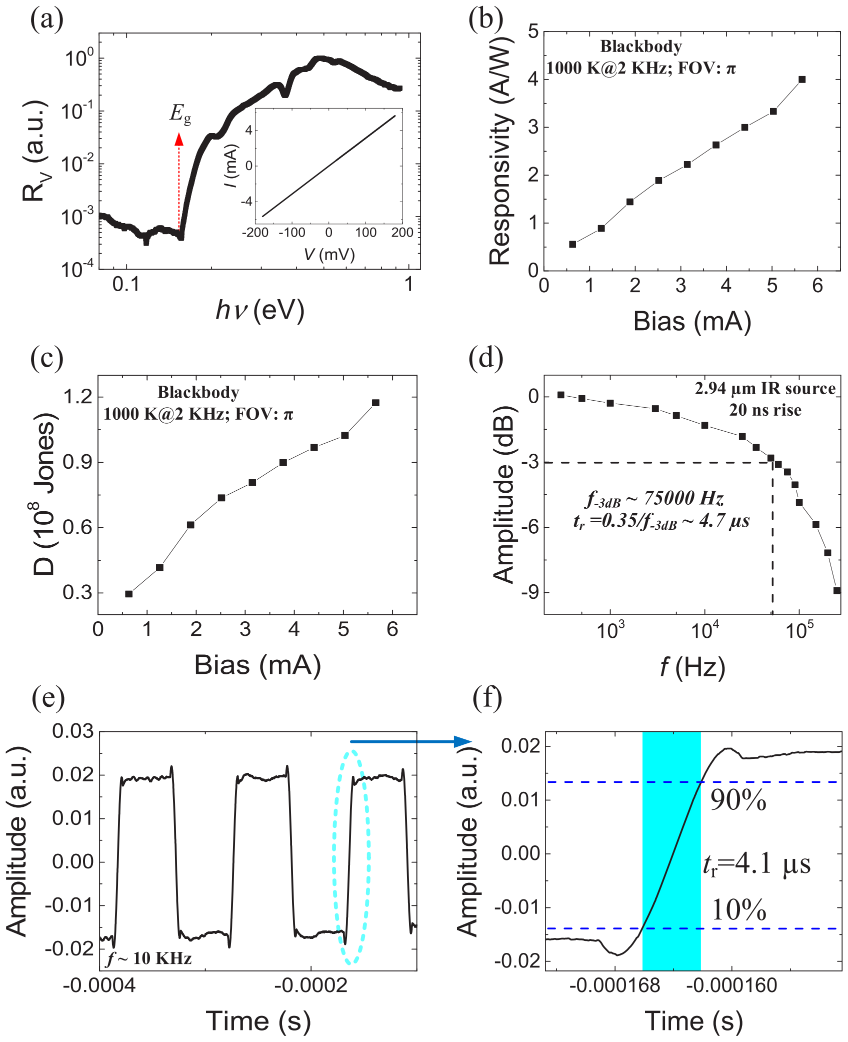

Fig. 3. (a) Spectral response of the detector at IR range. The inset is the typical current-voltage characteristic curve of the detector. (b-c) Blackbody responsivity (b) and Detectivity (c) of the device at different bias current. (d) Amplitude-frequency response of the detector in IR range. (e) The typical response waveform of the detector at 2.94 μm. (f) Rise speed of the detector at 2.94 μm.

Figure 4(a) shows the voltage responsivity of the detector at 167 GHz (1.796 mm) under different bias current up to 25 mA. The millimeter source is electrically modulated with a frequency of 10 KHz. As shown, under lower bias, the responsivity increases linearly with the increasing of bias. But it tends to saturation while further increasing the bias to high level. This is due to the gradually saturated electron velocity in InSb [17,31]. At 5 mA, the responsivity is 7 V/W and it increases to 25 V/W when the bias is 25 mA. But if we consider the real active semiconductor area, the corresponding responsivity of the detector is 389 V/W and 1389 V/W at 5 mA and 25 mA, respectively. The NEP decreases as increasing the bias but finally saturated between 20-25 mA due to the increased noise level (Fig. 4(b)), which has been plotted in inset of Fig. 4(b). At 167 GHz, the lowest NEP of the detector is about 1×10^{-10} W$\text{Hz}^{-1/2}$, which is comparable to the commercial Golay cell and pyroelectric detectors, but not as good as SBDs. But if we consider the real active semiconductor area of the detector, the NEP can reach to 1.8×10^{-12} W$\text{Hz}^{-1/2}$, which is comparable with or even superior to that of SBDs, for example, model WR6.5 ZBD from VDI (1.1×10^{-11} W$\text{Hz}^{-1/2}$) [35].

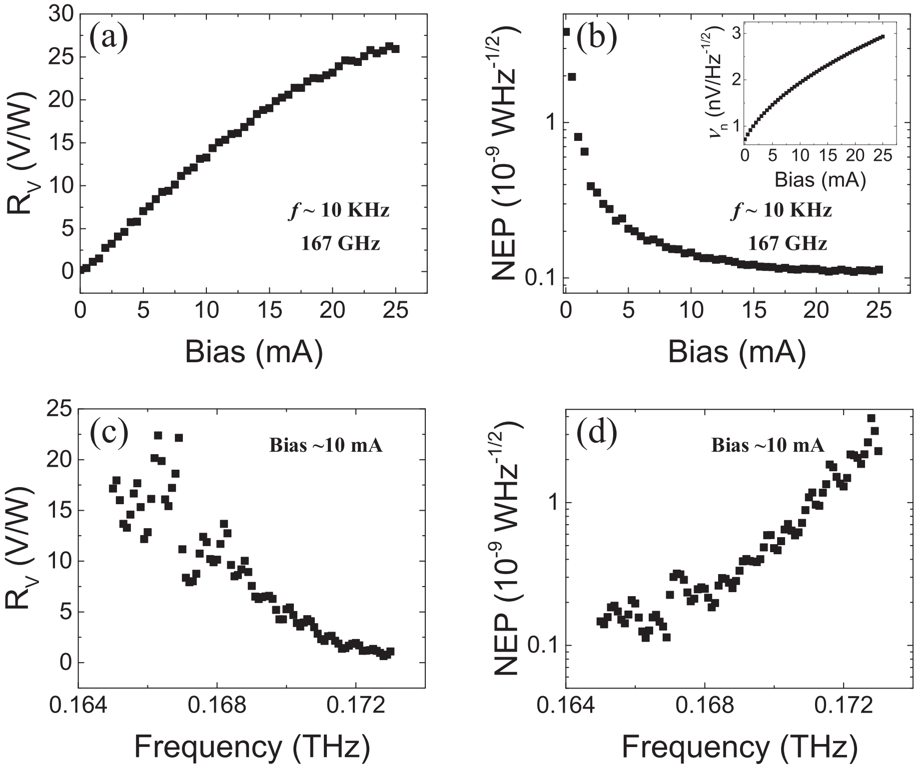

Fig. 4. Responsivity (a) and NEP (b) of the detector as functions of bias current under 167 GHz radiation. Spectral responsivity (c) and NEP (d) of the detector under radiations from 164 GHz to 174 GHz under a bias current of 10 mA.

The spectral response of the detector at around 167 GHz was characterized under a bias current of 10 mA. As shown in Fig. 4(c), the highest responsivity occurs at 166 GHz. The small deviation from 167 GHz is due to the fabrication. By increasing the radiation frequency to 173 GHz, the responsivity gradually decreases to very lower level. Therefore, this detector with the specialized spiral antenna design exhibits a high frequency cutoff at 173 GHz. This character is mainly determined by the narrow-band coupling capability of the spiral antenna. Normally, an antenna possesses an optimal coupling frequency range and the coupling efficiency will be significantly decreased beyond it. For example, for the simple dipole-type antenna, it usually has a high coupling efficiency at L=λ/2 (named half-wave antenna, L is the total length of the antenna and λ is the coupled wavelength) [17,25]. For the corresponding NEP (Fig. 4(d)), it has the lowest value at 166 GHz and then increases as increasing of the radiation frequency up to 173 GHz. The value at 173 GHz is already 1-2 order higher than that at 166 GHz, indicating the coupling efficiency decreases 1-2 order of magnitude.

We also characterized the response speed of the detector in millimeter wave by measuring its amplitude-frequency response. As shown in Fig. 5(a), it has a $f_{\text{-3dB}}$ value of 17.5 KHz, corresponding to a detector rise time of 20 µs, which is much faster than commercial Golay cell and pyroelectric detectors. As shown in the inset, the Golay cell only has a $f_{\text{-3dB}}$ value of 15 Hz and a rise time of 23 ms, three orders of magnitude slower than that of InSb detector. To further verify, we plot the typical response waveform of the detector at 167 GHz with a modulation frequency of 10 KHz. A rise time of 20 µs is also observed (Figs. 5(b) and 5(c)).

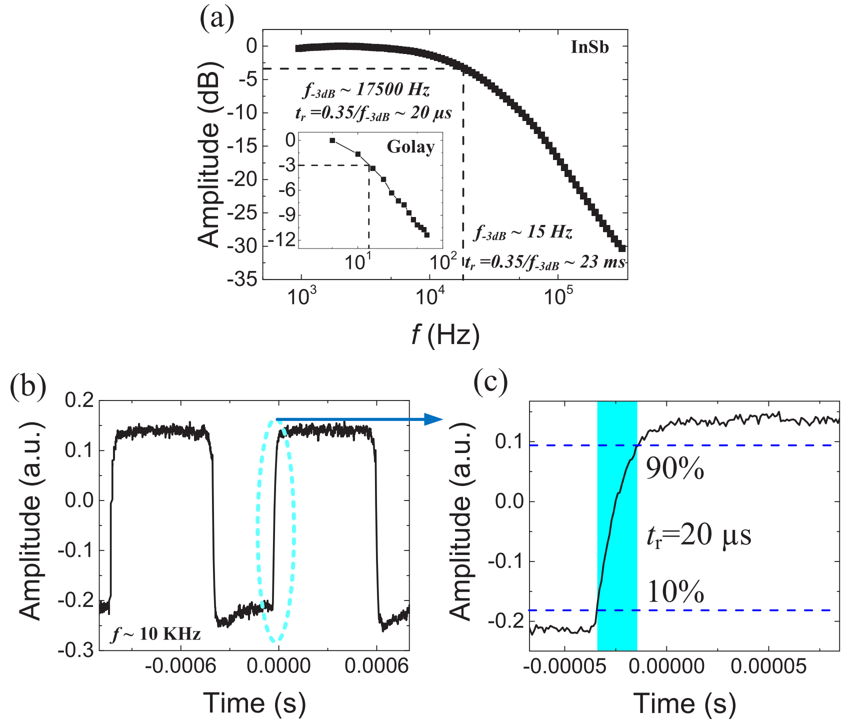

Fig. 5. (a) Amplitude-frequency response of the detector at 167 GHz. The inset is the Amplitude-frequency response of the Golay cell detector under the same radiation. (b) Typical response waveform of the detector to the 167 GHz radiations with modulation frequency of 10 KHz. (c) Rise time of the detector.

From above experiments, the detector demonstrates its capability of dual-band photoresponse in IR and millimeter waves. As the photoresponse to millimeter wave comes from the plasmonic effect in InSb, which possesses a negative dielectric constant according to Drude model [36,37]

$$\varepsilon(\omega) = \varepsilon_\infty \varepsilon_0 [1 - {\omega_p}^2/(\omega^2 + i\omega\omega_\tau)], \tag{4}$$

where ε_∞ is the high-frequency permittivity, ω_τ is the average collision rate of the charge carriers, and ε_0 is the permittivity in vacuum. By changing the dielectric property of InSb, the plasmonic effect will be modulated, resulting in modified photoresponse. The plasma frequency ω_p is defined as

$${\omega_p}^2 = q^2 n/(m^* \varepsilon_\infty \varepsilon_0), \tag{5}$$

where, q is the elementary charge, n is the electron density, and m^* is the effective electron mass. As such, the plasma frequency would be modulated if we can change the carrier concentration in InSb. To achieve this, we can use optical or IR pumping to excite interband transition in InSb, which would lead to increasing of the electron concentration therefore increase the plasma frequency according to Eq. (5). In experiments, we used a 1064 nm continuous laser with adjustable output power to pump InSb to change the plasma frequency and further the negative permittivity of InSb in millimeter wave. In such way, the intensity of excited LSP will be changed, resulting in changing of number of nonequilibrium photoconductive electrons.

As shown in Fig. 6(a), when we gradually increase the current (output power) of the laser from 0 up to maximum 3.4 A, the photovoltage of the detector gradually reduces. This is observed at different radiation frequency from 164 GHz to 174 GHz. Figure 6(b) plots the photovoltage as a function of laser current (power) at 167 GHz. By increasing the laser current from 0 to 3 A, the photovoltage decreases from ~0.08 mV to ~0.05 mV. To gain an insight on this decrease, we fit it with an exponentially decay function

$$y = Aexp(-x/B)\ + C, \tag{6}$$

The fitting shows that a base photovoltage of $C = 0.042$ mV is achieved, representing the output while increasing the laser power to infinite. As the generation of photoexcited electrons is limited by the density of states, the carrier concentration cannot be kept increase to infinite. Therefore, a maximum modulation depth of 47.5% can be achieved. To have a qualitatively insight, we simulate the plasmonic intensity within InSb at different plasma frequency (Details regarding our simulations can be seen from our previous report [17,23]). As shown in Fig. 6(c), the intensity gradually decreases while increasing the plasma frequency from $\omega_{\rm p0}$ to $7\omega_{\rm p0}$. The reduced plasmonic intensity reflects the reduced photoconductive electrons induced from LSPs, which is

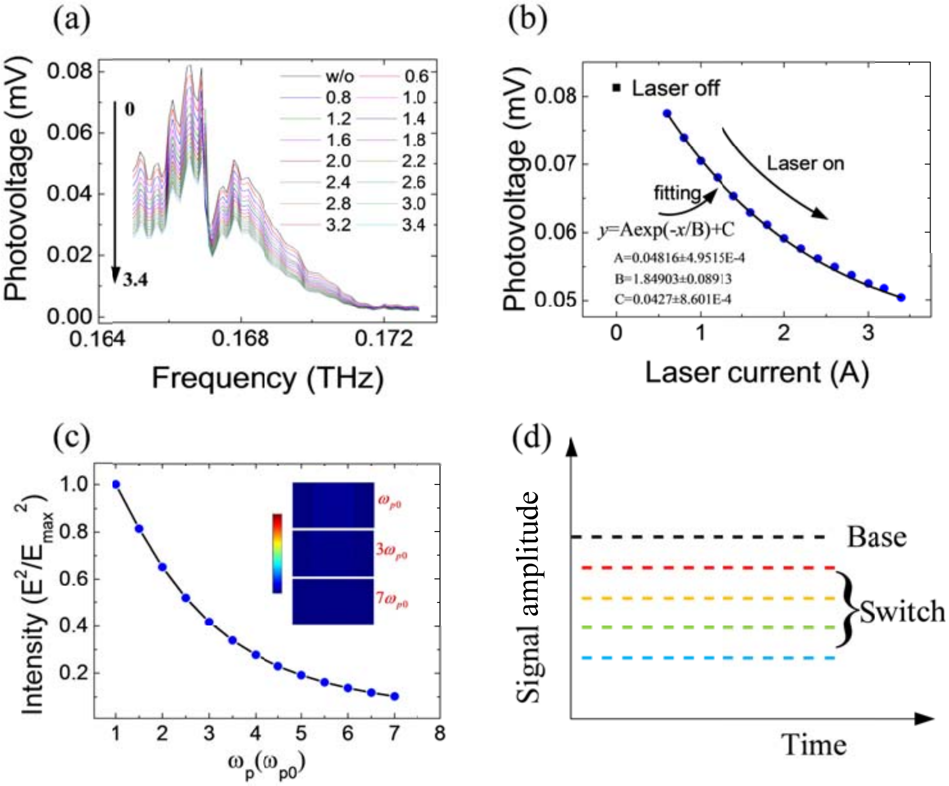

Fig. 6. (a) Spectral response of the detector from 164 GHz to 174 GHz under pumping of 1064 nm IR laser with different pumping power (different laser current). (b) The photovoltage signal of the detector at 167 GHz under different pumping power. (c) The simulated plasmonic intensity distribution at different plasma frequency. (d) Schematic of IR-millimeter switch by using this detector.

consistent with the photovoltage reduction with respect to pump laser power in Figs. 6(a) and 6(b). It is note that we only give a proof-of-principle here for this IR modulated photoresponse for millimeter wave of this dual-band detector. This capability links the two detectable wavelength range, which has potential to be used in broadband electromagnetic wave from IR to millimeter such as an IR-millimeter switch as conceptually shown in Fig. 6(d) [38,39]. Further study on this modulation and its application needs to be conducted in future work.

3. Conclusions

All-InSb film-based uncooled photodetector with capability of dual-band detection in IR and millimeter waves has been studied. The performance of this detector in the dual-band is comparable with or even superior to commercially available counterparts. Specifically, the detector exhibits a specific detectivity of $\sim 1\times10^{8}$ Jones and NEP of 1×10^{-10} $\mathrm{WHz}^{-1/2}$ at IR and millimeter, respectively. The NEP up to 1.8×10^{-12} $\mathrm{WHz}^{-1/2}$ can be achieved if consider the real active semiconductor area in the device. The detector also demonstrates fast response speed in both bands. This dual-band detection strategy in simple InSb on sapphire offers a promising pathway to pursue next generation of photodetection. Infrared-modulated photoresponse to millimeter wave is also demonstrated, which would inspire novel optoelectronic device in the two bands.

Funding

Agency for Science, Technology and Research (SERC 1720700038, SERC A1883c0002); Ministry of Education - Singapore (RG177/17); National Natural Science Foundation of China (61604160, 61625505).

Acknowledgement

The first author would like to thank the support of Nanyang Technological University Presidential Postdoctoral Fellowship.

Disclosures

The authors declare no conflicts of interest.

References

1. A. Rogalski, *Infrared Detectors* (CRC, 2010).
2. P. Klipstein, ""XBn" barrier photodetectors for high sensitivity and high operating temperature infrared sensors," in *Infrared Technology and Applications XXXIV*, B. F. Andresen, G. F. Fulop, and P. R. Norton, eds. (2008), 6940 (April 2008), p. 69402U.
3. A. Haddadi, A. Dehzangi, R. Chevallier, S. Adhikary, and M. Razeghi, "Bias–selectable nBn dual–band long–/very long–wavelength infrared photodetectors based on InAs/InAs$_{1-x}$Sb$_x$/AlAs$_{1-x}$Sb$_x$ type–II superlattices," Sci. Rep. **7**(1), 3379 (2017).
4. J. Chu and A. Sher, *Device Physics of Narrow Gap Semiconductors* (Springer New York, 2010).
5. C. Jagadish, S. Gunapala, and R. David, *Advances in Infrared Photodetectors* (Elsevier, 2011).
6. I. McKerracher, J. Wong-Leung, G. Jolley, L. Fu, H. H. Tan, and C. Jagadish, "Selective Intermixing of InGaAs/GaAs Quantum Dot Infrared Photodetectors," IEEE J. Quantum Electron. **47**(5), 577–590 (2011).
7. G. Jolley, L. Fu, H. H. Tan, and C. Jagadish, "Influence of quantum well and barrier composition on the spectral behavior of InGaAs quantum dots-in-a-well infrared photodetectors," Appl. Phys. Lett. **91**(17), 173508 (2007).
8. D. Palaferri, Y. Todorov, A. Bigioli, A. Mottaghizadeh, D. Gacemi, A. Calabrese, A. Vasanelli, L. Li, A. G. Davies, E. H. Linfield, F. Kapsalidis, M. Beck, J. Faist, and C. Sirtori, "Room-temperature nine-µm-wavelength photodetectors and GHz-frequency heterodyne receivers," Nature **556**(7699), 85–88 (2018).
9. D. Hofstetter, M. Beck, and J. Faist, "Quantum-cascade-laser structures as photodetectors," Appl. Phys. Lett. **81**(15), 2683–2685 (2002).
10. B. Schwarz, P. Reininger, A. Harrer, D. MacFarland, H. Detz, A. M. Andrews, W. Schrenk, and G. Strasser, "The limit of quantum cascade detectors: A single period device," Appl. Phys. Lett. **111**(6), 061107 (2017).

11. A. Jollivet, B. Hinkov, S. Pirotta, H. Hoang, S. Derelle, J. Jaeck, M. Tchernycheva, R. Colombelli, A. Bousseksou, M. Hugues, N. Le Biavan, J. Tamayo-Arriola, M. Montes Bajo, L. Rigutti, A. Hierro, G. Strasser, J.-M. Chauveau, and F. H. Julien, "Short infrared wavelength quantum cascade detectors based on m-plane ZnO/ZnMgO quantum wells," Appl. Phys. Lett. **113**(25), 251104 (2018).
12. V. I. Shashkin, V. L. Vaks, V. M. Danil'tsev, A. V. Maslovsky, A. V. Murel, S. D. Nikiforov, O. I. Khrykin, and Y. I. Chechenin, "Microwave Detectors Based on Low-Barrier Planar Schottky Diodes and Their Characteristics," Radiophys. Quantum Electron. **48**(6), 485–490 (2005).
13. A. Semenov, O. Cojocari, H.-W. Hübers, F. Song, A. Klushin, and A.-S. Müller, "Application of Zero-Bias Quasi-Optical Schottky-Diode Detectors for Monitoring Short-Pulse and Weak Terahertz Radiation," IEEE Electron Device Lett. **31**(7), 674–676 (2010).
14. B. Szentpáli, P. Basa, P. Fürjes, G. Battistig, I. Bársony, G. Károlyi, T. Berceli, V. Rymanov, and A. Stöhr, "Thermopile antennas for detection of millimeter waves," Appl. Phys. Lett. **96**(13), 133507 (2010).
15. C. W. Berry, N. Wang, M. R. Hashemi, M. Unlu, and M. Jarrahi, "Significant performance enhancement in photoconductive terahertz optoelectronics by incorporating plasmonic contact electrodes," Nat. Commun. **4**(1), 1622 (2013).
16. K. Peng, P. Parkinson, L. Fu, Q. Gao, N. Jiang, Y.-N. Guo, F. Wang, H. J. Joyce, J. L. Boland, H. H. Tan, C. Jagadish, and M. B. Johnston, "Single Nanowire Photoconductive Terahertz Detectors," Nano Lett. **15**(1), 206–210 (2015).
17. J. Tong, W. Zhou, Y. Qu, Z. Xu, Z. Huang, and D. H. Zhang, "Surface plasmon induced direct detection of long wavelength photons," Nat. Commun. **8**(1), 1660 (2017).
18. "640 × 512 Indium antimonide (InSb) MWIR infrared camera," http://www.ircameras.com/camera/irc906hs.
19. V. Giannini, A. Berrier, S. A. Maier, J. A. Sánchez-Gil, and J. G. Rivas, "Scattering efficiency and near field enhancement of active semiconductor plasmonic antennas at terahertz frequencies," Opt. Express **18**(3), 2797 (2010).
20. X. Wang, A. A. Belyanin, S. A. Crooker, D. M. Mittleman, and J. Kono, "Interference-induced terahertz transparency in a semiconductor magneto-plasma," Nat. Phys. **6**(2), 126–130 (2010).
21. L. Deng, J. Teng, H. Liu, Q. Y. Wu, J. Tang, X. Zhang, S. A. Maier, K. P. Lim, C. Y. Ngo, S. F. Yoon, and S. J. Chua, "Direct Optical Tuning of the Terahertz Plasmonic Response of InSb Subwavelength Gratings," Adv. Opt. Mater. **1**(2), 128–132 (2013).
22. S. M. Hanham, A. I. Fernández-Domínguez, J. H. Teng, S. S. Ang, K. P. Lim, S. F. Yoon, C. Y. Ngo, N. Klein, J. B. Pendry, and S. A. Maier, "Broadband Terahertz Plasmonic Response of Touching InSb Disks," Adv. Mater. **24**(35), OP226–OP230 (2012).
23. J. Tong, Y. Qu, F. Suo, W. Zhou, Z. Huang, and D. H. Zhang, "Antenna-assisted subwavelength metal–InGaAs–metal structure for sensitive and direct photodetection of millimeter and terahertz waves," Photonics Res. **7**(1), 89 (2019).
24. P. Tcheg, K. D. Bello, and D. Pouhe, "A planar equiangular spiral antenna array for the V-/W-band," in *2017 11th European Conference on Antennas and Propagation (EUCAP)* (IEEE, 2017), pp. 1148–1152.
25. C. A. Balanis, *Antenna Theory: Analysis and Design*, 3rd ed. (John Wiley & Sons: New York, 2005).
26. J. Dyson, "The equiangular spiral antenna," IRE Trans. Antennas Propag. **7**(2), 181–187 (1959).
27. M. McFadden and W. R. Scott, "Analysis of the Equiangular Spiral Antenna on a Dielectric Substrate," IEEE Trans. Antennas Propag. **55**(11), 3163–3171 (2007).
28. S. Tretyakov, "Maximizing Absorption and Scattering by Dipole Particles," Plasmonics **9**(4), 935–944 (2014).
29. F. Sizov and A. Rogalski, "THz detectors," Prog. Quantum Electron. **34**(5), 278–347 (2010).
30. M. Zerbini, A. Doria, G. P. Gallerano, E. Giovenale, and G. Galatola-Teka, "Far Infrared and THz Detectors: Principles of Operation and Figures of Merit," in *2018 43rd International Conference on Infrared, Millimeter, and Terahertz Waves (IRMMW-THz)* (IEEE, 2018), pp. 1–2.
31. S. M. Sze, *Physics of Semiconductor Devices*, Environmental Science and Engineering (Springer International Publishing, 2014).
32. "InSb photoconductive detectors," https://www.hamamatsu.com/jp/en/product/optical-sensors/infrared-detector/insb-photoconductive-detector/index.html
33. K. Lau, A. Lakhani, R. S. Tucker, and M. C. Wu, "Enhanced modulation bandwidth of nanocavity light emitting devices," Opt. Express **17**(10), 7790 (2009).
34. K. Wertheim, "Carrier Lifetime in Indium Antimonide," Phys. Rev. **104**(3), 662–664 (1956).
35. "VDI detectors" https://www.vadiodes.com/en/products/detectors
36. S. Lin, K. Bhattarai, J. Zhou, and D. Talbayev, "Thin InSb layers with metallic gratings: a novel platform for spectrally-selective THz plasmonic sensing," Opt. Express **24**(17), 19448 (2016).
37. E. D. Palik, *Handbook of Optical Constants of Solids II* (Academic, 1991).
38. N. Henry, D. Burghoff, Q. Hu, and J. B. Khurgin, "Temporal characteristics of quantum cascade laser frequency modulated combs in long wave infrared and THz regions," Opt. Express **26**(11), 14201 (2018).
39. L. Zhang, K. Mu, Y. Zhou, H. Wang, C. Zhang, and X.-C. Zhang, "High-power THz to IR emission by femtosecond laser irradiation of random 2D metallic nanostructures," Sci. Rep. **5**(1), 12536 (2015).